NATIONAL UNIVERSITY OF SINGAPORE

Understanding the brightness and heralding efficiency of down conversion sources

by

Wang Xiande, Samuel

A thesis submitted in partial fulfillment for the
degree of Bachelor of Science (Honours) in Physics

in the
Faculty of Science
Department of Physics

April 2015

Abstract

Ever since its discovery, the optical process of spontaneous parametric down conversion (SPDC) has been widely researched and has come to be extensively used, especially in the design of entangled photon or single photon sources. Numerous models of SPDC have been created over the years, with various assumptions and limitations to the applicability of their results.

In this thesis, a particular SPDC source design is studied and ray tracing is performed to model the coupling of the down-converted photons into the collection fibre. The optimal parameters for the pump beam as well as the collection optics design are determined to optimise the brightness of the source. The results are then compared with the collected spectra reported from other sources.

Acknowledgements

I would like to express my sincere gratitude to my project supervisor Prof Alexander Ling for his support throughout this project. His patient and encouraging guidance has sparked my interest in optics and has never failed to raise my morale and offer a new path when I am lost and unsure of what to do in the project.

Special thanks to Brigitta for offering her help so generously in answering my numerous questions and explaining the experiment. Her care and support helped me to pull through the difficult moments of the semester.

Finally, my family has been the unwavering source of comfort and encouragement in my life. Thanks for all the understanding and unconditional love, for nurturing me and allowing me to pursue my interests. It is truly my great privilege to have you as family.

Contents

Chapter 1

Introduction

Spontaneous parametric down conversion (SPDC) is a nonlinear optical process in which correlated photons are produced. It is the process at the heart of numerous single photon sources or entangled photon sources. These sources have, in turn, enabled numerous advances in fundamental physics and the field of quantum optics, such as tests of Bell's inequality [1] and implementations of a variety of quantum technologies, from quantum teleportation [2] to quantum cryptography [3] and quantum imaging [4]. More recently, generation of higher dimensional entangled states [5–7] have been explored.

1.1 Motivation

A workhorse process for generating single photons, SPDC has attracted intense theoretical interest [8–12] to better understand the down-conversion sources and to develop optimisation methods. However, as a testament to the complexity of the system, no complete theory accounting for every variable has been derived, nearly 50 years after its discovery. An SPDC set up contains a myriad of variables, from the geometry and focus of the beams to the thickness of the crystal and the type of pump beam used (pulsed or continuous wave) giving rise to many different configurations to study and different parameters to optimise for.

Instead of tackling the full complexity of the general derivations head on, a simplified classical approach with geometric ray tracing is adopted to make it easier to account for more variables of the set up. Although the results will only be approximate due to the simplified treatment, it is hoped that the main features of the system will be retained and that the model developed in this thesis can provide useful, albeit approximate, suggestions for optimising a down-conversion source.

1.2 Scope

This thesis has two main parts. In the first part the theory of nonlinear optics will be introduced with the relevant nonlinear processes and effects explained. The model of the down-conversion source will then be developed in the following chapter and certain interesting results highlighted. A comparison of the predicted spectrum will also be done with measurements obtained from other sources and the use of a cylindrical lens to compensate for spatial walk-off effects will be studied before the thesis is concluded.

Chapter 2

Nonlinear optics

Nonlinear optics is the study concerned with the effects caused by optical media that have nonlinear response to applied electromagnetic (EM) fields. The basic principles of nonlinear optics have already been established by the 1960s [13, 14] and experimental progress closely followed advances in optical crystal fabrication and the newly invented laser technology to provide the high intensity EM fields needed for the polarisation of the optical crystals to enter the nonlinear regime. The nonlinear response of the optical medium means that the superposition principle no longer applies which leads to a host of nonlinear processes like frequency mixing that allows for applications like the generation of frequencies not directly available from a laser source.

2.1 Nonlinear polarisation

In an isotropic dielectric medium, the polarisation density P, defined as the average electric dipole moment per unit volume of the medium, can be expressed as a Taylor series of the applied electric field E.

$$P = \epsilon_0 (\underbrace{\chi^{(1)} E}_{\text{linear term}} + \underbrace{\chi^{(2)} E^2 + \chi^{(3)} E^3 + \ldots}_{\text{nonlinear terms}})$$

where ϵ_0 is the permittivity of free space, $\chi^{(1)}$ is the linear susceptibility and $\chi^{(2)}, \chi^{(3)}$ are the second- and third-order nonlinear susceptibilities. The electric susceptibilities here are just scalars due to the assumed isotropy of the medium.

Linear optics considers only the first term, which is a suitable approximation at low optical intensities as the optical field is much weaker than that within the atoms and molecules of the medium. This treatment is insufficient at higher intensities however, and higher order terms are included which leads to a rich and fascinating array of nonlinear effects. Under non-resonant conditions, perturbation theory can be used to derive the nonlinear susceptibilities [15]. It turns out that the nonlinear coefficients are dependent on the frequencies of the participating fields and hence are not constants even for processes of the same order.

2.2 Anisotropic medium

Generalising the treatment in the previous section to anisotropic media, the polarisation **P** and applied field **E** are now vectors while the nth order susceptibilities are tensors of rank $n + 1$.

$$\mathbf{P} = \epsilon_0(\chi^{(\mathbf{1})}\mathbf{E} + \chi^{(\mathbf{2})}\mathbf{EE} + \chi^{(\mathbf{3})}\mathbf{EEE} + \ldots) \tag{2.1}$$

Substituting this expression into the constitutive relation for the electric displacement $\mathbf{D} = \epsilon_0\mathbf{E} + \mathbf{P}$ and neglecting the higher order terms yields

$$\mathbf{D} = \epsilon_0\epsilon\mathbf{E} \tag{2.2}$$

where $\epsilon = \mathbf{I} + \chi^{(\mathbf{1})}$ is the dielectric tensor.

The ϵ tensor can be shown to be real and symmetric in a lossless medium [16], hence it can be diagonalised with purely real eigenvalues. This simplifies the relation in matrix form to

$$\begin{pmatrix} D_x \\ D_y \\ D_z \end{pmatrix} = \epsilon_0 \begin{pmatrix} \epsilon_{xx} & 0 & 0 \\ 0 & \epsilon_{yy} & 0 \\ 0 & 0 & \epsilon_{zz} \end{pmatrix} \begin{pmatrix} E_x \\ E_y \\ E_z \end{pmatrix} = \epsilon_0 \begin{pmatrix} n_x^2 & 0 & 0 \\ 0 & n_y^2 & 0 \\ 0 & 0 & n_z^2 \end{pmatrix} \begin{pmatrix} E_x \\ E_y \\ E_z \end{pmatrix} \tag{2.3}$$

and the orthogonal basis vectors are known as the principal axes and n_i refers to the refractive index of a light wave polarised along the i principal axis. Isotropic media will have all three refractive indices equal, while media with two equal indices ($\epsilon_{xx} = \epsilon_{yy}$) and all different indices are classified as uniaxial and biaxial respectively.

2.3 Plane wave solutions

To study the propagation of light in birefringent media, we consider plane wave solutions of the Maxwell equations for nonmagnetic media with no free changes

$$\nabla \cdot \mathbf{B} = 0 \tag{2.4a}$$

$$\nabla \cdot \mathbf{D} = 0 \tag{2.4b}$$

$$\nabla \times \mathbf{E} = -\frac{\partial \mathbf{B}}{\partial t} \tag{2.4c}$$

$$\nabla \times \mathbf{H} = \frac{\partial \mathbf{D}}{\partial t} \tag{2.4d}$$

where $\mathbf{B}$ and $\mathbf{H}$ are the magnetic field with $\mathbf{B} = \mu_0 \mathbf{H}$ and all the four vectors have the dependence $e^{i(\mathbf{k}\cdot\mathbf{r}-\omega t)}$.

For such waves to satisfy the Maxwell equations, Fresnel's equation

$$\left(\frac{1}{n_y^2}-\frac{1}{n^2}\right)\left(\frac{1}{n_z^2}-\frac{1}{n^2}\right)k_x^2+\left(\frac{1}{n_x^2}-\frac{1}{n^2}\right)\left(\frac{1}{n_z^2}-\frac{1}{n^2}\right)k_y^2+\left(\frac{1}{n_x^2}-\frac{1}{n^2}\right)\left(\frac{1}{n_y^2}-\frac{1}{n^2}\right)k_z^2=0$$

must hold [17], which shows that two refractive indices n are allowed for any direction of $\hat{\mathbf{k}}$. For example, for $\hat{\mathbf{k}} = (1, 0, 0)$, $n = n_y$ or n_z.

To determine the refractive index for an arbitrary direction of $\mathbf{k}$, we introduce the index ellipsoid. Consider the surface of constant energy density $U = \mathbf{E} \cdot \mathbf{D}$. Using Equation (2.3),

$$U = \frac{D_x^2}{\epsilon_0 n_x^2} + \frac{D_y^2}{\epsilon_0 n_y^2} + \frac{D_z^2}{\epsilon_0 n_z^2}$$

Let $U = 1/\epsilon_0$, then

$$\frac{D_x^2}{n_x^2} + \frac{D_y^2}{n_y^2} + \frac{D_z^2}{n_z^2} = 1$$

which specifies an ellipsoid with semi-axis lengths of n_x, n_y and n_z. The intersection between the ellipsoid and the plane perpendicular to the $\mathbf{k}$ vector forms an ellipse, which can be shown [18] to have several useful properties.

First, the major and minor axes of the ellipse gives the two allowed orthogonal directions of $\mathbf{D}$. For a birefringent medium, where $n_x = n_y$, one of the allowed directions of $\mathbf{D}$ always lies on the x-y plane, while the other allowed direction depends on the angle between $\mathbf{k}$ and the z-axis.

Second, the lengths of the axes of the ellipse gives the refractive indices for the wave with that $\mathbf{D}$ and $\mathbf{k}$ vector directions. For a birefringent medium, since one of the allowed directions of $\mathbf{D}$ lies in the x-y plane, which intersects the ellipsoid in a circle, the refractive index $n_o (= n_x = n_y)$ for this polarisation is the same for all directions of **k** and is called the ordinary-, or o-wave. The other allowed polarisation is called the extraordinary-, or e-wave and its refractive index n_e is given by

$$n_e(\theta) = \left(\frac{\cos^2\theta}{n_x^2} + \frac{\sin^2\theta}{n_z^2} \right)^{-1/2} \tag{2.5}$$

where θ is the angle between the **k** vector and the z-axis. Note that when $\theta = 0$ (**k** lies along the z-axis), $n_e = n_o$ which means that the refractive index is independent of polarisation. Thus the z-axis is known as the optic axis.

2.4 Walk-off effect

We shall now proceed to get a better picture of the directions of the electric and magnetic field vectors involved and understand the walk-off effect, which is an important phenomenon for propagation of light in nonlinear media.

Without loss of generality, we set the z-axis along the **k** vector. Equation (2.4a) then becomes

$$\frac{\partial B_z}{\partial z} = 0 \tag{2.6}$$

which implies that $B_z = 0$ and hence **B** (and **H**) lies in the x-y plane. In the same way, Equation (2.4b) implies that **D** also lies in the x-y plane.

Now let the y-axis be along the **B** and **H** vectors, so that $\mathbf{H} = H\hat{\mathbf{y}}$ and $\mathbf{B} = B\hat{\mathbf{y}}$. Equation (2.4d) thus becomes

$$-\frac{\partial H}{\partial z}\hat{\mathbf{x}} = \frac{\partial \mathbf{D}}{\partial t} \tag{2.7}$$

which implies that **D** lies along the x-axis.

Similarly, Equation (2.4c) simplifies to

$$-\frac{\partial E_y}{\partial z}\hat{\mathbf{x}} + \frac{\partial E_x}{\partial z}\hat{\mathbf{y}} = -\frac{\partial B}{\partial t}\hat{\mathbf{y}} \tag{2.8}$$

which implies that $E_y = 0$ and hence **E** lies in the x-z plane. The precise direction of **D** is specified by the constitutive relation (Equation (2.2)) and is in general not parallel to **E**.

The results of these deductions are shown in the Figure 2.1. We see that **H**, **D** and **k** are mutually orthogonal and the Poynting vector $\mathbf{S} = \mathbf{E} \times \mathbf{H}$ does not coincide with the **k** vector. The Poynting vector gives the direction of energy flow of the wave, hence an extraordinary wave will walk away from an ordinary wave with the same **k** vector, as shown in Figure 2.2.

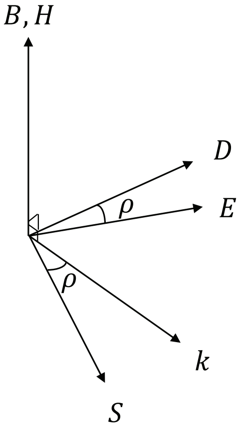

Figure 2.1: Directions of the various fields of an EM plane wave

In birefringent media, the walk-off effect only occurs for extraordinary waves as ordinary waves have **D** vectors in the x-y plane ($D_z = 0$) and thus from Equation (2.3), **D** is parallel to **E**, so the **k** and **S** vectors are collinear.

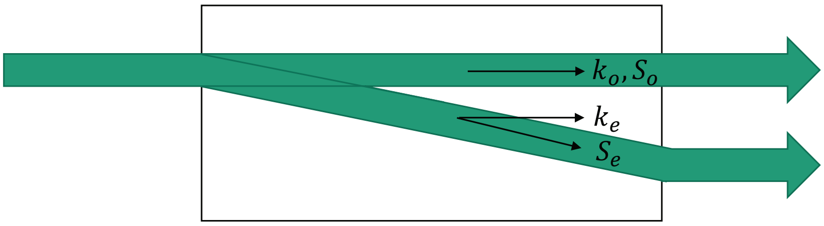

Figure 2.2: Spatial walk-off of e-wave in birefringent crystal

The walk-off angle ρ is typically on the order of several degrees and is given by

$$\rho(\theta) = \tan^{-1}\left(\frac{n_o^2}{n_e^2}\tan(\theta)\right) - \theta \tag{2.9}$$

where θ is the angle between $\mathbf{k}_e$ and the optic axis.

The spatial walk-off effect has important consequences for nonlinear processes involving interactions between multiple waves of different polarisations as the waves gradually get physically separated from each other which reduces their effective interaction distance within the crystal. This is more pronounced when working with focused beams with small spot sizes and methods to minimise the effect include using two or more crystals with different orientations to allow the beams to walk back and continue their interaction [19, 20].

2.5 Nonlinear processes

The origin of nonlinear optical processes is the nonlinear terms in the polarisation (Equation (2.1)) which allows for frequency mixing between the input waves to occur. As an example, we consider the interaction of two linearly polarised one-dimensional plane waves. The input to the crystal is then

$$E = \frac{1}{2}A_1 e^{i(k_1 z - \omega_1 t)} + \frac{1}{2}A_2 e^{i(k_2 z - \omega_2 t)} + cc.$$

The second order polarisation is then

$$\begin{aligned} P^{(2)} = \frac{1}{2}\epsilon_0 \chi^{(2)} \Big(& A_1^2 e^{i(2k_1 z - 2\omega_1 t)} + A_2^2 e^{i(2k_2 z - 2\omega_2 t)} \\ & + A_1^{*\,2} e^{-i(2k_1 z - 2\omega_1 t)} + A_2^{*\,2} e^{-i(2k_2 z - 2\omega_2 t)} \\ & + |A_1|^2 + |A_2|^2 \\ & + A_1 A_2^* e^{i((k_1 - k_2)z - (\omega_1 - \omega_2)t)} + A_1^* A_2 e^{i((k_2 - k_1)z - (\omega_2 - \omega_1)t)} \\ & + A_1 A_2 e^{i((k_1 + k_2)z - (\omega_1 + \omega_2)t)} + A_1^* A_2^* e^{-i((k1 + k_2)z - (\omega_1 + \omega_2)t)} \Big) \end{aligned}$$

The interaction between the two waves produces optical fields where the frequencies are the possible sums and differences of the input waves.

To find the wave equation for three-wave processes in birefringent media, we consider linearly polarised ordinary and extraordinary waves and begin from Maxwell's equations by taking the curl of Equation (2.4b) and using Equation (2.4d):

$$\nabla \times (\nabla \times \mathbf{E}) = -\mu_0 \frac{\partial \mathbf{D}^2}{\partial t^2} \tag{2.10}$$

From Equation (2.3),

$$\begin{aligned} \nabla \cdot \mathbf{D} &= \epsilon_0 (n_x^2 \frac{\partial}{\partial x} E_x + n_y^2 \frac{\partial}{\partial y} E_y + n_z^2 \frac{\partial}{\partial z} E_z) \\ &= \epsilon_0 n_x^2 [\nabla \cdot \mathbf{E} + (\frac{n_z^2}{n_x^2} - 1) \frac{\partial}{\partial z} E_z] \end{aligned}$$

But since $\nabla \cdot \mathbf{D} = 0$ (Equation (2.4a)),

$$\nabla \cdot \mathbf{E} = (1 - \frac{n_z^2}{n_x^2}) \frac{\partial}{\partial z} E_z \approx 0$$

for weak birefringence ($n_x \approx n_z$). This approximation becomes exact for ordinary waves since $E_{z,\text{ord}} = 0$.

Finally, applying the vector identity $\nabla \times (\nabla \times \mathbf{E}) = \nabla(\nabla \cdot \mathbf{E}) - \nabla^2\mathbf{E}$ on the left side of Equation (2.10), we get

$$\begin{aligned} \nabla^2\mathbf{E} &= \mu_0 \frac{\partial^2\mathbf{D}}{\partial t^2} \\ &= \mu_0 \left(\epsilon_0 \frac{\partial^2\mathbf{E}}{\partial t^2} + \frac{\partial^2\mathbf{P}^{\mathrm{L}}}{\partial t^2} + \frac{\partial^2\mathbf{P}^{\mathrm{NL}}}{\partial t^2} \right) \end{aligned} \tag{2.11}$$

where the constitutive relation for the electric displacement was used and the polarisation was split into linear and nonlinear terms.

Each frequency will now be considered separately. The nonlinear polarisation will contain frequencies not present in the inputs as shown in the example earlier in this section, however we shall consider only the nonlinear polarisation term for the frequencies of interest. This is permissible as the weak nonlinear polarisations will not interact significantly with each other.

Let us choose the difference frequency generation (DFG) process as an example. This process involves two input waves of frequencies ω_1 and ω_2 producing a wave of frequency $\omega_3 = \omega_1 - \omega_2$. The fields for frequency ω_3 are

$$\begin{aligned} \mathbf{E} &= \frac{1}{2}\mathbf{A}'_3 e^{-i\omega_3 t} + cc. \\ \mathbf{P}^{\mathrm{L}} &= \frac{1}{2}\epsilon_0 \chi^{(1)} \mathbf{A}'_3 e^{-i\omega_3 t} + cc. \\ \mathbf{P}^{\mathrm{NL}} &= \frac{1}{2}\mathbf{P}^{(2)} e^{-i\omega_3 t} + cc. \end{aligned}$$

which, by substituting into Equation (2.11), yields

$$\nabla^2\mathbf{A}'_3 = -\frac{\omega_3^2 n_3^2}{c^2}\mathbf{A}'_3 - \omega_3^2\mu_0\mathbf{P}^{(2)} \tag{2.12}$$

We now separate the complex amplitude $\mathbf{A}'(\mathbf{r}) = \mathbf{A}(\mathbf{r})e^{i\mathbf{k}\cdot\mathbf{r}}$ into its envelope $\mathbf{A}(\mathbf{r})$ and the oscillating factor $e^{i\mathbf{k}\cdot\mathbf{r}}$ to get the ith component of $\nabla^2\mathbf{A}'_3$

$$(\nabla^2\mathbf{A}'_3)_i = e^{i\mathbf{k}\cdot\mathbf{r}}(\nabla^2 A_{3,i} + 2i\mathbf{k}\cdot\nabla A_{3,i} - \mathbf{k}^2 A_{3,i}) \tag{2.13}$$

Combining Equation (2.12) and (2.13), the equation for a linearly polarised wave can be simplified to

$$2i\mathbf{k}_3 \cdot \nabla A_{3,i} e^{i\mathbf{k}_3\cdot\mathbf{r}} = -\omega^2\mu_0\mathbf{P}_i^{(2)} \tag{2.14}$$

where the equation now applies for plane waves of a given frequency, and the slowly varying envelope approximation (SEVA) which assumes $\mathbf{A}$ varies slowly over a wavelength and so $|\mathbf{k}\cdot\nabla A_i| \gg |\nabla^2 A_i|$ has been applied. To carry on the calculation further requires the nonlinear polarisation $\mathbf{P}^{(2)}$ to be determined.

2.6 Second-order nonlinear polarisation

In the general treatment for second order processes involving three waves, the second order nonlinear susceptibility $\chi^{(2)}$ is a third rank tensor and so the polarisation is given by

$$P_i^{(2)}(\omega_m,\omega_n) = \frac{\epsilon_0}{4}\sum_{m,n}\sum_{j,k}\chi_{ijk}^{(2)}(\omega_m+\omega_n;\omega_m,\omega_n)A'_j(\omega_m)A'_k(\omega_n)e^{-i(\omega_m+\omega_n)t}$$

where $\mathbf{A}(\omega)$ is the electric field complex amplitude of the wave with frequency ω and the input frequencies are ω_m and ω_n.

This is a complicated equation with 27 components of the susceptibility tensor, multiplied by 2 for the complex conjugate terms. But it turns out that the expression can be greatly simplified through the exploitation of various symmetries. For frequencies far away from resonances, the medium is lossless and so the susceptibility components are real and the complex conjugate terms simply requires a negation of the frequencies. Thus the summation indices m and n include only the negative and positive of each frequency involved in the process.

Next, keeping only the terms with frequencies relevant to the chosen process, neglecting the dispersion of $\chi^{(2)}$, and applying various permutation symmetries, the details of which are covered in numerous textbooks [15, 17], we arrive at an expression involving a process-specific column vector multiplied by a d-tensor. For a DFG process, written in a contracted notation, the result is

$$\mathbf{P}^{(2)}(\omega_1-\omega_2) = 2\epsilon_0\begin{pmatrix} d_{11} & d_{12} & d_{13} & d_{14} & d_{15} & d_{16} \\ d_{16} & d_{22} & d_{23} & d_{24} & d_{14} & d_{12} \\ d_{15} & d_{24} & d_{33} & d_{23} & d_{13} & d_{14} \end{pmatrix}\begin{pmatrix} A'_x(\omega_1)A'^*_x(\omega_2) \\ A'_y(\omega_1)A'^*_y(\omega_2) \\ A'_z(\omega_1)A'^*_z(\omega_2) \\ A'_y(\omega_1)A'^*_z(\omega_2)+A'_z(\omega_1)A'^*_y(\omega_2) \\ A'_x(\omega_1)A'^*_z(\omega_2)+A'_z(\omega_1)A'^*_x(\omega_2) \\ A'_x(\omega_1)A'^*_y(\omega_2)+A'_y(\omega_1)A'^*_x(\omega_2) \end{pmatrix} \tag{2.15}$$

where the d-tensor components $d_{ijk} = \frac{1}{2}\chi_{ijk}^{(2)}$ and the contracted index notation is given in Table 2.1.

The number of independent components of the d-tensor have thus been reduced to 10. This can be further reduced through the consideration of crystal symmetry, which depends of the point group that the crystal belongs to. For example, beta barium borate

Contracted index	j, k
1	xx
2	yy
3	zz
4	yz, zy
5	xz, xz
6	xy, yx

TABLE 2.1: Contracted notation for j, k index of d-tensor

(BBO) is a uniaxial crystal with the point group 3m which has the d-tensor

$$\mathbf{d}_{\text{BBO}} = \begin{pmatrix} 0 & 0 & 0 & 0 & d_{31} & -d_{22} \\ -d_{22} & d_{22} & 0 & d_{31} & 0 & 0 \\ d_{31} & d_{31} & d_{33} & 0 & 0 & 0 \end{pmatrix}.$$

with the non-linear optical components d_{22} and d_{31} of about 2.1 and 0.15 pm/V respectively [21].

The components of the electric field complex amplitudes can be determined since typically only the ordinary $\hat{\mathbf{o}}$ and extraordinary $\hat{\mathbf{e}}$ directions are used. In the principal-axis coordinate system of the crystal, with the optic axis along the z-axis, the unit wave vector $\hat{\mathbf{k}}$, $\hat{\mathbf{o}}$ and $\hat{\mathbf{e}}$ can be determined with the help of Figure 2.3 to be

$$\begin{aligned} \hat{\mathbf{k}} &= \sin\theta\cos\phi\hat{\mathbf{x}} + \sin\theta\sin\phi\hat{\mathbf{y}} + \cos\theta\hat{\mathbf{z}} \\ \hat{\mathbf{o}} &= \sin\phi\hat{\mathbf{x}} - \cos\phi\hat{\mathbf{y}} \\ \hat{\mathbf{e}} &= -\cos(\theta+\rho)\cos\phi\hat{\mathbf{x}} - \cos(\theta+\rho)\sin\phi\hat{\mathbf{y}} + \sin(\theta+\rho)\hat{\mathbf{z}} \end{aligned}$$

where θ, ϕ are the spherical coordinates of $\hat{\mathbf{k}}$ and ρ is the walk-off angle, which is added since the amplitudes in the column vector of Equation (2.15) are of the electric field.

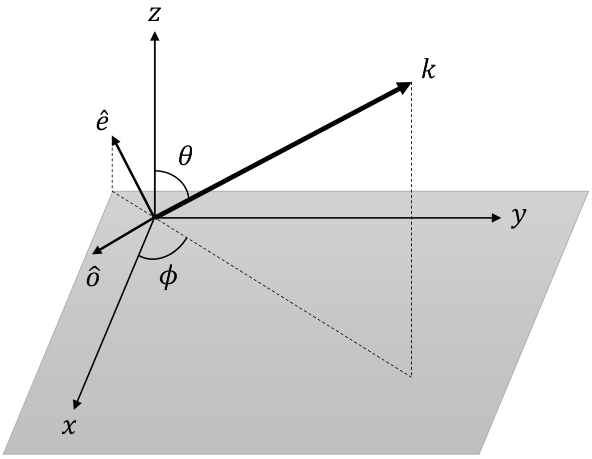

FIGURE 2.3: Direction of e- and o-waves

With the complex amplitudes of the o- and e- polarised input electric fields $\mathbf{A}_{1,2} = A_{1,2}\hat{\mathbf{o}}$ or $\hat{\mathbf{e}}$, we can now rewrite Equation (2.15) in the form

$$\mathbf{P}_i^{(2)}(\omega_1 - \omega_2) = 2\epsilon_0 d_{\text{eff,i}}(\theta, \phi) A_1(\omega_1) A_2^*(\omega_2)$$

in terms of a geometry-dependent effective nonlinearity column vector d_{eff}.

Finally, we project the polarisation $\mathbf{P}^{(2)}$ onto the polarisation direction of the third field, $\hat{\mathbf{o}}$ or $\hat{\mathbf{e}}$, to give the final result

$$P_{\text{DFG}}^{(2)}(\omega_1 - \omega_2) = 2\epsilon_0 d_{\text{eff}}(\theta, \phi) A_1(\omega_1) A_2^*(\omega_2) e^{i((\mathbf{k}_1 - \mathbf{k}_2)\cdot\mathbf{r}} \tag{2.16}$$

2.7 Coupled amplitude equations

Continuing where we left off at Equation (2.14), we use the nonlinear polarisation from Equation (2.16) and arrive at

$$2i\mathbf{k}_3 \cdot \nabla A_{3,i} e^{i\mathbf{k}_3\cdot\mathbf{r}} = -\frac{2\omega_3^2}{c^2} d_{\text{eff}} A_1 A_2^* e^{i(\mathbf{k}_1 - \mathbf{k}_2)\cdot\mathbf{r}},$$

which depends on the amplitudes of the two input fields A_1 and A_2. A_1 and A_2 are themselves functions of A_3 and each other, and have to be found by following a similar procedure as that used for A_3. We thus obtain the three coupled amplitude equations

$$\begin{aligned}
\nabla_{\hat{\mathbf{k}}_1} A_1 &= i\frac{\omega_1}{n_1 c} d_{\text{eff}} A_3 A_2 e^{-i\Delta\mathbf{k}\cdot\mathbf{r}} \\
\nabla_{\hat{\mathbf{k}}_2} A_2 &= i\frac{\omega_2}{n_2 c} d_{\text{eff}} A_1 A_3^* e^{i\Delta\mathbf{k}\cdot\mathbf{r}} \\
\nabla_{\hat{\mathbf{k}}_3} A_3 &= i\frac{\omega_3}{n_3 c} d_{\text{eff}} A_1 A_2^* e^{i\Delta\mathbf{k}\cdot\mathbf{r}}
\end{aligned}$$

where $\Delta\mathbf{k} = \mathbf{k}_1 - \mathbf{k}_2 - \mathbf{k}_3$ which is known as the phase matching condition.

We now make the assumption that A_1 and A_2 are constants. This is valid for small conversion efficiency such that there is no appreciable change to the input fields. This leaves us with just one differential equation that can be integrated directly:

$$\begin{aligned}
A_3 &= i\frac{\omega_3}{n_3 c} d_{\text{eff}} A_1 A_2^* \int_0^L e^{i\Delta\mathbf{k}\cdot\mathbf{r}} d\hat{\mathbf{k}}_3 \\
&= i\frac{2\omega_3}{\Delta k n_3 c} d_{\text{eff}} A_1 A_2^* e^{i\Delta\mathbf{k}\cdot\hat{\mathbf{k}}_3 L/2} \sin\Big(\Delta\mathbf{k}\cdot\hat{\mathbf{k}}_3 L/2\Big)
\end{aligned}$$

In terms of intensities, using $I = \frac{n}{2\mu_0 c}|A|^2$ for a plane wave,

$$I_3 = \frac{2\mu_0\omega_3^2 L^2}{n_1 n_2 n_3 c} d_{\text{eff}}^2 I_1 I_2 \,\text{sinc}^2\left(\frac{\Delta\mathbf{k}\cdot\hat{\mathbf{k}}_3 L}{2}\right) \tag{2.17}$$

The intensity of the difference frequency wave is thus proportional to $\text{sinc}^2(\frac{\Delta\mathbf{k}\cdot\hat{\mathbf{k}}_3 L}{2})$, which is called the phase matching efficiency term and varies from 0 to 1. The output intensity is thus critically dependent on maximising this term.

2.8 Phase matching

Phase matching is the attempt to ensure $\Delta k = 0$ so that the phase matching efficiency becomes as close to 1 as possible. Early observations of nonlinear processes [22] had extremely weak intensities due to the set up not being phase matched. For a three-wave process, phase matching is not easy to achieve. For example, in a normally dispersive media, where $n_1 > n_2 > n_3$ for waves of frequency $\omega_1 > \omega_2 > \omega_3$, phase matched collinear three-wave processes are impossible since

$$\begin{aligned}\Delta k &= \tfrac{1}{c}[n_1\omega_1 - n_2\omega_2 - n_3\omega_3] \\ &= \tfrac{1}{c}[\omega_2(n_1 - n_2) + \omega_3(n_1 - n_3)] > 0.\end{aligned} \tag{2.18}$$

For non-zero Δk, after propagating a distance $L_c = \pi/\Delta k$, known as the coherence length, the generated field becomes π out of phase with the input fields and destructive interference occurs, which causes the nonlinear process to go into reverse until the generated field gets depleted at $2L_c$ before the process reverses again.

There are several methods for achieving the phase matching conditions. In birefringent phase matching, a birefringent crystal is used and careful selection of the polarisation (ordinary or extraordinary) and propagation directions of the waves involved is done. There is an extra degree of freedom in changing the refractive indices since the refractive index of an extraordinary wave is a function of the angle formed by the wave vector with the optic axis. If a collinear geometry is desired, the directions of the waves are fixed but the crystal can still be rotated to change the refractive index of the extraordinary waves and phase matching can be achieved for certain frequency combinations.

The three types of birefringent phase matching are type 0, type I and type II. In type 0 phase matching, all three fields are polarised along the same direction, ordinary or extraordinary, while Type I phase matching has only the two output fields being polarised along the same direction (example: $e \rightarrow o + o$), and Type II phase matching involves two oppositely polarised output fields (example: $e \rightarrow e + o$).

The phase matching diagram for non-collinear interaction is shown in Figure 2.4. In the diagram, the propagation direction of the signal field k_2 forms an angle ψ with the pump beam direction k_1. The direction of $\mathbf{k}_3$ is assumed to be such that the magnitude of $\Delta\mathbf{k}$ is minimised, thus $\Delta\mathbf{k} \cdot \hat{\mathbf{k}}_3 = \Delta k$. Using various trigonometric relations, we can solve for the magnitude of $\Delta\mathbf{k}$:

$$\Delta\mathbf{k} = (\mathbf{k}_1^2 + \mathbf{k}_2^2 - 2\mathbf{k}_1\mathbf{k}_2 \cos\psi)^{1/2} - \mathbf{k}_3 \tag{2.19}$$

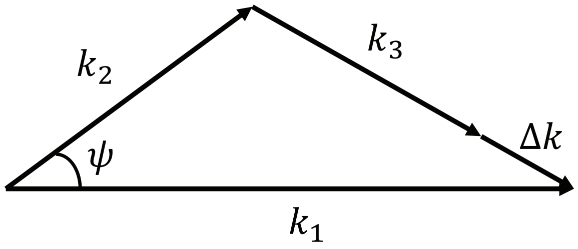

Figure 2.4: Phase matching diagram

There are also other methods of phase matching, including quasi phase matching which involve multiple crystal segments of alternating orientation (periodically poled crystals). The reversal of the orientation reverses the phase velocity of the generated field at regular intervals, thus ensuring that the destructive interference does not occur [23].

2.9 Spontaneous parametric down conversion

SPDC is the process by which a photon undergoes spontaneous disintegration into a pair of photons under the conditions of conservation of energy and momentum (Figure 2.5). First observed in the mid 1960s [24–26], theoretical studies rapidly followed [27–30] which developed the understanding of the fundamental processes behind SPDC and is still an active area of research today.

SPDC is widely used in many quantum optics experiments in entangled photon sources, which rely on the correlations between the two down-converted photons. The down-converted photons have spatial, spectral, temporal and polarisation correlations, and photons entangled in every degree of freedom (hyperentanglement [31]) have been produced [32]. The spatial and energy-time correlations come from the momentum and energy conservation laws respectively, while the polarisation correlation is due to the birefringent phase matching.

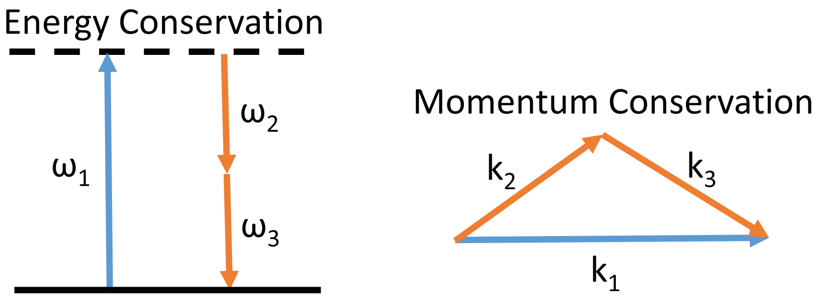

FIGURE 2.5: Energy and momentum conservation

The basic SPDC set up (Figure 2.6) is made of an input beam, called the pump beam, impinging onto a birefringent crystal with $\chi^{(2)}$ nonlinearity. The pump beam couples with the vacuum modes of the crystal and two daughter beams are created, called the signal for the beam with the target frequency and the idler for the other beam.

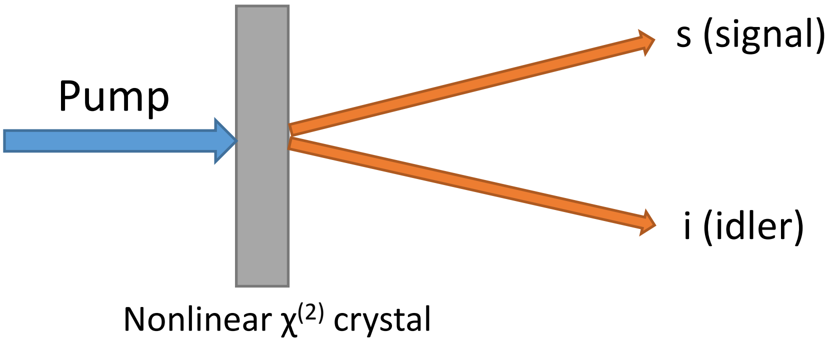

FIGURE 2.6: SPDC

This process is somewhat similar to DFG where two beams, the pump and the signal, are present at the input to the crystal and the pump get split into a beam with the frequency of the signal and another beam with the frequency equal to the difference between the pump and the signal, thus amplifying the signal in the process. The difference between the two processes is that for SPDC, the input signal beam has zero amplitude, thus the frequency of the signal beam is not fixed and the pump can be split into a range of frequency combinations as long as frequency and momentum are conserved. The process occurs due to the coupling of the pump beam with the vacuum modes in the crystal. Modes which are better phase matched will have a higher transition amplitude and hence have higher intensity. Due to the lack of a strong signal beam for the pump beam to couple with, the conversion efficiency is very low at about 10^{-9} [9]. This down-conversion occurs spontaneously and randomly throughout the crystal and thus can only approximate a deterministic photon source [33].

SPDC sources can be classified according to their geometry, down-converted frequencies and phase matching type. There are two types of geometries, collinear and non-collinear, which refer to the spatial modes of the signal and idler beams. For instance, the geometry shown in Figure 2.6 is non-collinear. Non-collinear geometry has the advantage of differentiable spatial modes for the signal and idler beams to be separated, however photon sources that have collinear geometry have a simpler set up. The frequencies of the signal and idler can either be degenerate (having the same frequency) or non-degenerate (different frequencies), while for the phase matching type, there are three possibilities, type 0, type I or II which are described earlier in Section 2.8.

The SPDC source design that will be the focus of this study is taken from Trojek [34]. This source produces polarisation-entangled photon pairs and is based on the two-crystal design first implemented in 1999 [35] and was chosen due to its compactness and simplicity afforded by the collinear geometry as well as its high brightness compared to other conventional crystal designs. The conceptual layout of the source is shown in Figure 2.7.

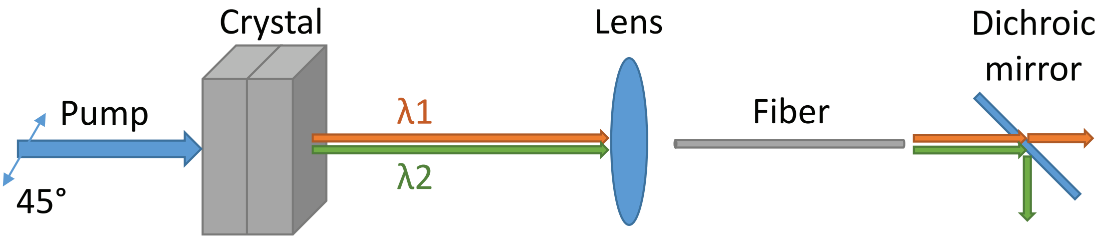

FIGURE 2.7: Simple, compact and robust polarisation-entangled photon source

A pump beam linearly polarised at 45° is incident onto two BBO crystals placed adjacent to each other. The BBO crystals are oriented such that both crystals satisfy the type I collinear phase matching conditions for the desired down-converted frequencies $\lambda 1$ and $\lambda 2$ but with the optic axis of one of the crystals in the horizontal direction while the optic axis of the other crystal lies in the vertical direction. This allows down-conversion to occur in either crystal with equal probability and thus an polarisation-entangled state $|\psi\rangle = |H\rangle_1 |H\rangle_2 + e^{i\phi} |V\rangle_1 |V\rangle_2$, where $|H\rangle$ and $|V\rangle$ are the horizontal and vertical polarisation states, is produced. The down-converted photons are then collected into a single mode fiber which directs the light to a dichroic mirror that separates the path of the two photons to their respective detectors.

Chapter 3

Model

We seek now to create a mathematical model of the chosen down-conversion source described in the previous chapter. The main modification that will be made to the design is the use of only one BBO crystal instead of two adjacent crystals. This means that the source will not produce polarisation-entangled photons but only polarisation-correlated photons. We shall begin by making certain simplifying assumption while still preserving the main features of the physical process. There will be two parts to the modelling – the SPDC process itself that occurs within the BBO crystal and the collection optics that couples the down-converted light into the fiber. A possible method to compensate for the walk-off effect of the pump beam is then examined.

3.1 Crystal

A classical treatment is used for the down-conversion in the crystal. Although SPDC is a process stimulated by quantum vacuum fluctuations and so a full quantum mechanical treatment is needed to find the absolute brightness of the source, it turns out that the classical treatment leads to the same dependence on the phase matching efficiency for the simplified model that is developed here. The pump, signal and idler beams are approximated as monochromatic plane waves with the pump beam normally incident onto the crystal. Under the weak signal assumption, where the intensity of the pump and idler beams are undepleted, the intensity of the signal I_3 is given by Equation (2.17):

$$I_{3,\text{abs}} = \frac{2\mu_0 \omega_3^2 L^2}{n_1 n_2 n_3 c} d_{\text{eff}}^2 I_1 I_2 \operatorname{sinc}^2\left(\frac{\Delta\mathbf{k}\cdot\hat{\mathbf{k}}_3 L}{2}\right)$$

and the intensity relative to the maximum

$$I_3 = \frac{I(\Delta\mathbf{k})}{I(\Delta\mathbf{k}=0)} = \mathrm{sinc}^2\left(\frac{\Delta\mathbf{k}\cdot\hat{\mathbf{k}}_3 L}{2}\right). \tag{3.1}$$

In this section and the next, we will be using a pump frequency $\lambda_1 = 405$ nm, signal frequency $\lambda_2 = 785$ nm and idler frequency $\lambda_3 = 837$ nm. To ensure the phase matching condition for type I ($e \to o + o$) collinear down-conversion, the tilt angle θ, which is the angle between the wave vector of the pump beam and the optic axis of the crystal, such that $\Delta k = 0$ had to be determined. From Equation (2.19)

$$\Delta k = 2\pi\left(\frac{n_e(\lambda_1,\theta)}{\lambda_1} - \frac{n_o(\lambda_2)}{\lambda_2} - \frac{n_o(\lambda_3)}{\lambda_3}\right) \tag{3.2}$$

where n_o and n_e are the refractive indices for the ordinary and extraordinary fields.

The refractive indices were determined as follows: the ordinary refractive index $n_o = n_x$ and the extraordinary index n_e is given by Equation (2.5), which is a function of n_x, n_z and θ, the angle between the optic axis of the crystal and the z-axis (pump beam direction). n_x and n_z are functions of wavelength and are obtained from the Sellmeier equations for BBO [17]

$$\begin{aligned} n_x &= \sqrt{2.7359 + \frac{0.01878}{\lambda^2 - 0.01822} - 0.01354\lambda^2} \\ n_z &= \sqrt{2.3753 + \frac{0.01224}{\lambda^2 - 0.01677} - 0.01516\lambda^2} \end{aligned}$$

where the wavelength λ is given in μm.

The Newton-Raphson method was then used to numerically solve for $\Delta k = 0$ and the appropriate value of θ was found to be 28.8048°.

With the crystal fixed at the collinear phase matching conditions, we can now determine the relative intensity of signal at non-collinear conditions. Since the signal and idler beams are of ordinary polarisation, the non-collinear emission for each emission angle will be in cones with the axis collinear with the propagation direction of the pump beam. The procedure to find the signal intensity is similar to the collinear case, just with a change of the equation for momentum mismatch $\mathbf{\Delta k}$ to

$$\mathbf{\Delta k} = 2\pi\left[\left(\frac{n_e(\lambda_1,\theta)}{\lambda_1}^2 + \frac{n_o(\lambda_2)}{\lambda_2}^2 - 2\frac{n_e(\lambda_1,\theta)}{\lambda_1}\frac{n_o(\lambda_2,\theta)}{\lambda_2}\cos\phi\right)^{1/2} - \frac{n_o(\lambda_3)}{\lambda_3}\right] \tag{3.3}$$

and then using (3.1) to find the relative intensity as a function of emission angle.

3.2 Collection beam

To couple the emitted light to the single-mode fiber, an achromatic doublet lens was used to reduce chromatic aberrations from the two non-degenerate emission wavelengths. Ray tracing was done to trace the propagation of the emitted light. This is justified as although the fiber guides a Gaussian transverse mode, at distances beyond several Rayleigh lengths from the focus, the Gaussian beam closely resembles a circular wave with the point source at the center of the focus. Another issue is that the achromatic doublet lens, being made of two lenses joined together, is quite thick and the thin lens approximation that simplifies the calculation cannot be applied. Thus ray tracing is performed for the light path within the lens as well.

Determining whether a ray gets coupled into the fiber can be done by checking that it lies within the acceptance cone of the fiber, given the distances between the crystal, lens and fiber. However this procedure is not used in practice as it is difficult to measure accurately the distance between the crystal, the lens and the fiber. The usual experimental method of maximising the collection efficiency is to match the emitted light to the mode of the fiber. This is done by shining light out from the fiber and through the lens, noting the position and size of the beam waist, and then positioning the center of the crystal at that point. Instead of using the acceptance angle of the fiber, we could use the divergence angle $\phi = \lambda/\pi\omega_0$, where ω_0 is the radius of the beam waist and λ is the frequency of the Gaussian beam, to determine the acceptance cone for the emissions from the crystal. The beam radius is measured to the distance where the intensity of the beam is $1/e^2$, or 13.5%, of the maximum intensity.

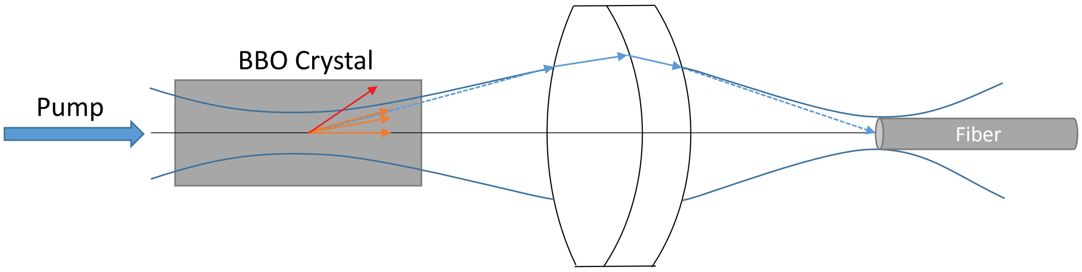

Figure 3.1: Model of SPDC set up

The diagram of the model is shown in Figure 3.1. A point source is assumed at the center of the BBO crystal. Since the center of the crystal coincides with the position of the collection beam waist, the acceptance of an emitted ray can be determined simply by checking if the emission angle is within the divergence angle of the collection beam. For example, the orange arrows in the figure represent rays that are accepted into the fiber while the red arrow is not accepted as it lies beyond the divergence angle of the beam, marked by the dashed blue line.

3.3 Results

The results of Section 3.1 allows us to find the joint spectrum which is the relative intensities of the various wavelengths and emission angles. For a crystal of length 15.76mm oriented for optimal collinear down-conversion of 405 nm light to 785 nm and 837 nm, the plot of the joint spectrum is shown in Figure 3.2.

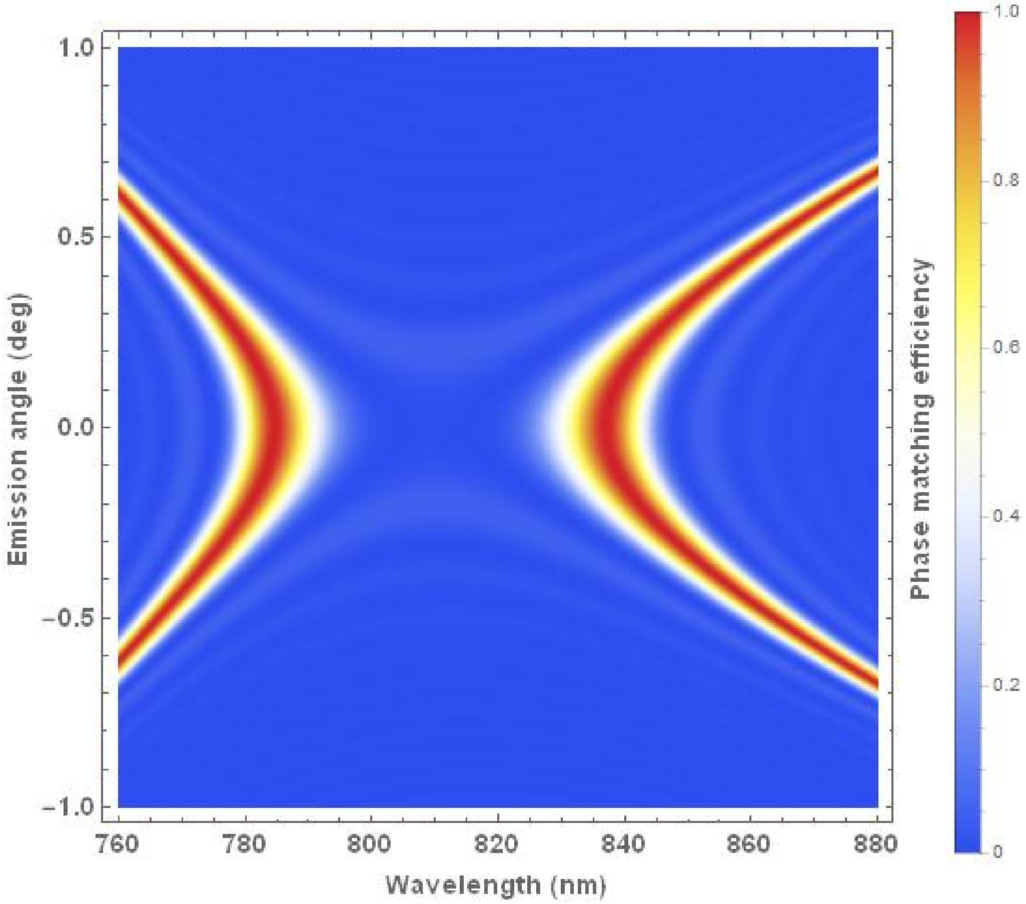

FIGURE 3.2: Joint spectrum at collinear phase matching conditions for 405 nm down-converted to 785 nm and 837 nm, crystal cut at 28.8048°

From the model developed in Section 3.2, in addition to the collinear emissions, light emitted at an angle up to the divergence angle of the collection beam will be accepted into the fiber. Thus to determine the relative total intensity, we perform an integration of the phase matching efficiency over emission angle ϕ within the maximum admission angle ϕ_0

$$I_{\text{total}}(\lambda) = \int_{-\phi_0}^{\phi_0} \text{sinc}^2(\Delta k L/2)\, d\phi \tag{3.4}$$

The integration was done numerically using the trapezoid rule (refer to the appendix for details) and the result is shown in Figure 3.3 for various integration limits.

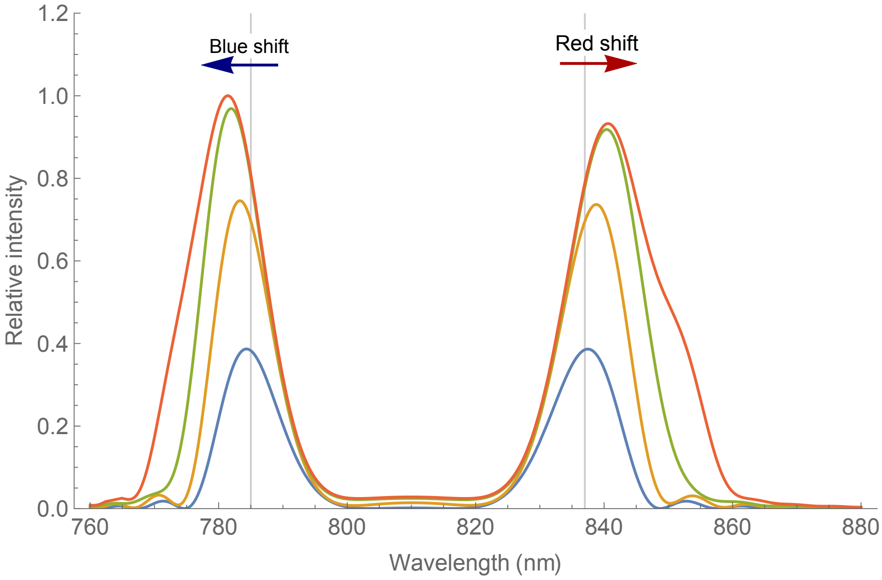

Figure 3.3: Relative brightness (arbitrary unit) integrated over emission angles of 0.1° (blue), 0.2° (yellow), 0.3° (green) and 0.4° (red)

The figure shows three effects as the acceptance angle of the collection fiber increases: the increase of intensity, shifting of wavelength at maximum intensity and broadening of the peaks. The intensity increase is due to the additional acceptance of light emitted at larger angles. As the maximum accepted emission angle increases, the increase in intensity gets smaller, thus there will be a maximum acceptance angle beyond which the collected intensity saturates.

The broadening and shift of the peaks can be explained by the shape of the joint spectrum where the peak wavelengths at non-zero emission angles shift away from the peak wavelengths at the collinear case. The full width at half maximum (FWHM) of the signal and idler peaks in the collected spectrum are shown in Figure 3.4. The FWHM of the signal (785 nm) is consistently smaller than that of the idler (837 nm) beam, which is also to be expected from the asymmetric shape of the joint spectrum.

The shift of the signal peak wavelength compared to that of the collinear emission is plotted as a function of acceptance angle in Figure 3.5. Similar to the increase of intensity, the shift of the peak collected wavelength reaches a maximum beyond a acceptance angle of about 0.36°.

There is another interesting implication of this result. The experimental procedure that is used to adjust the crystal to satisfy the collinear phase matching conditions for the desired wavelengths is to position the crystal at the waist of the collection beam and then place a spectral filter in the path of the collection beam after the crystal that

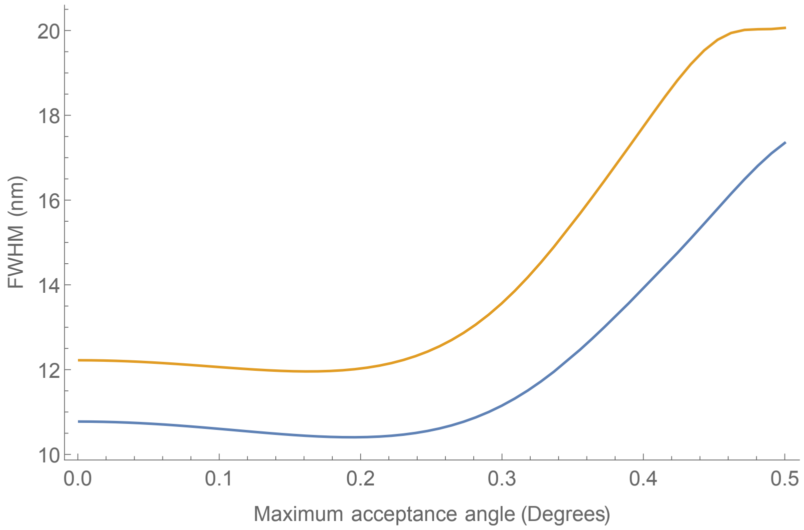

Figure 3.4: Full width at half maximum of signal (blue) and idler (yellow) beam spectrum

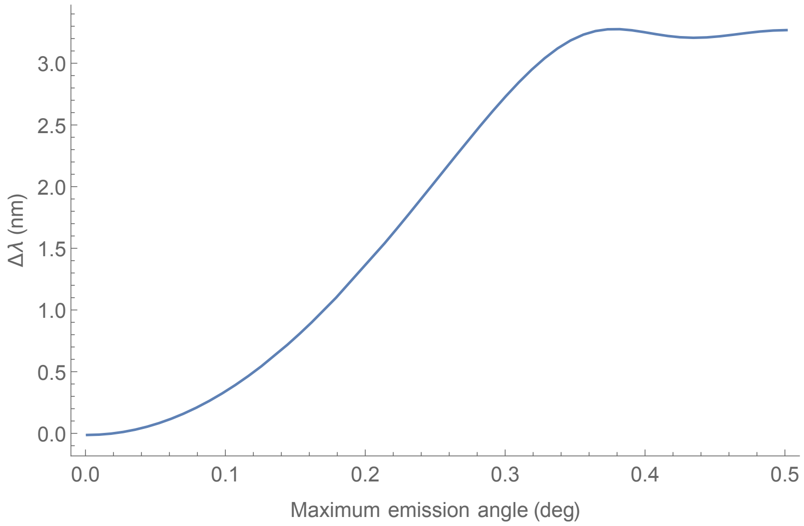

Figure 3.5: Shift in signal peak collected wavelength as acceptance angle increases becomes roughly constant at about 0.36°

allows only the signal wavelength to pass. The crystal is then carefully tilted until the maximum intensity is detected. If we assume that only the signal wavelength gets passed through the filter and that only the collinearly emitted light is collected, this approach will allow the crystal to be positioned at the precise phase matching angle that is desired. However, in practice the filter has a finite bandwidth and some of the non-collinearly emitted light is collected as well. Thus there is a shift in the intensity profile of the collected spectrum as established previously. We shall now examine the significance of this effect. We assume a constant detection efficiency for wavelengths within the filter bandwidth. The divergence angle of the collection beam is set at 0.4° and the filter is assumed to transmit perfectly only wavelengths from 780nm to 790nm. The total relative collected intensity as a function of crystal tilt angle θ is given by

$$I_{\text{total}}(\theta) = \int_{780\text{nm}}^{790\text{nm}} \int_{\text{-}0.4^\circ}^{0.4^\circ} \text{sinc}^2(\Delta k L/2)\, d\phi\, d\lambda \tag{3.5}$$

The maximum collected intensity was determined by finding the root of the derivative of Equation (3.5) and the corresponding tilt angle was 28.8094°. This differs from the target tilt angle of 28.8048° by 0.0046° which has an appreciable impact on the joint spectrum. As an illustration of this impact, the spectral profile of the collinearly-emitted light is shown in Figure 3.6 and for the emission within 0.4° in Figure 3.7.

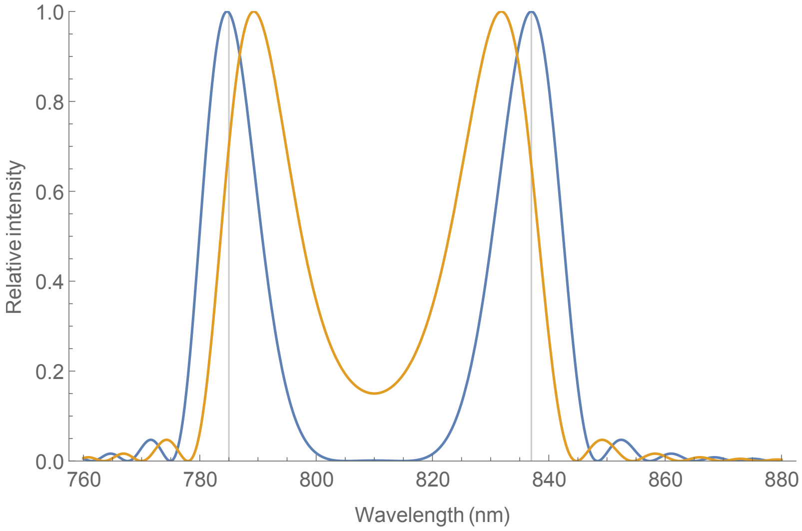

FIGURE 3.6: Collinear emission at ideal crystal angle satisfying collinear phase matching conditions (blue) and at crystal angle after the crystal alignment procedure (yellow)

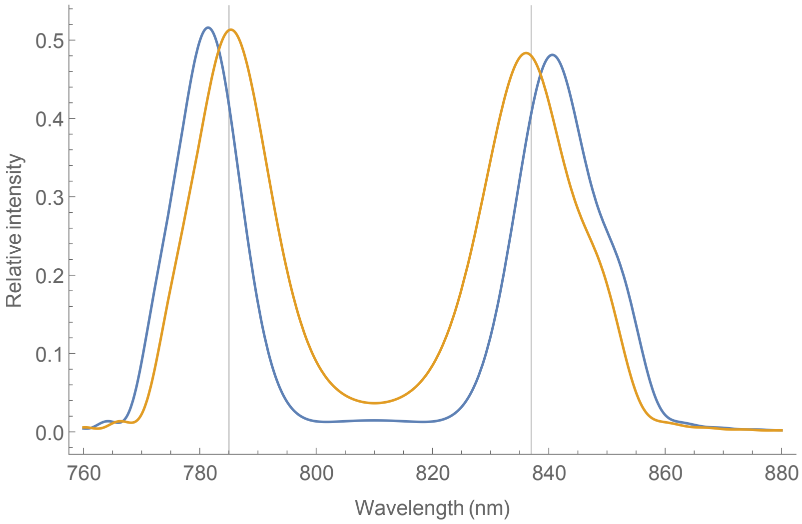

FIGURE 3.7: Integrated emission over 0.4° at ideal crystal angle satisfying collinear phase matching conditions (blue) and at crystal angle after the crystal alignment procedure (yellow)

The plots show a shift in the peak wavelengths and a broadening of the peaks in both the collinear emission (Figure 3.6) and integrated emission (Figure 3.7) such that the two peaks merge near the base between them and the intensity does not get quite close to zero. This merging of the two peaks could reduce slightly the separability of the signal and idler beams as the spectral separation of the two beams are reduced. The result thus suggests that filter of smaller bandwidths and collection beams of smaller divergence angles should be used during alignment of the crystal tilt to ensure that the tilt angle gets adjusted as close to the target angle as possible.

3.4 Comparison

We shall now compare the results of the model to the measured spectrum from two BBO, collinear, type I sources. The first source uses a 6 mm long BBO crystal and has target wavelengths of 760 nm and 867 nm with pump wavelength of 405 nm. The spectrum data was obtained from Tang ZK which was normalised separately for each peak and plotted in Figure 3.8.

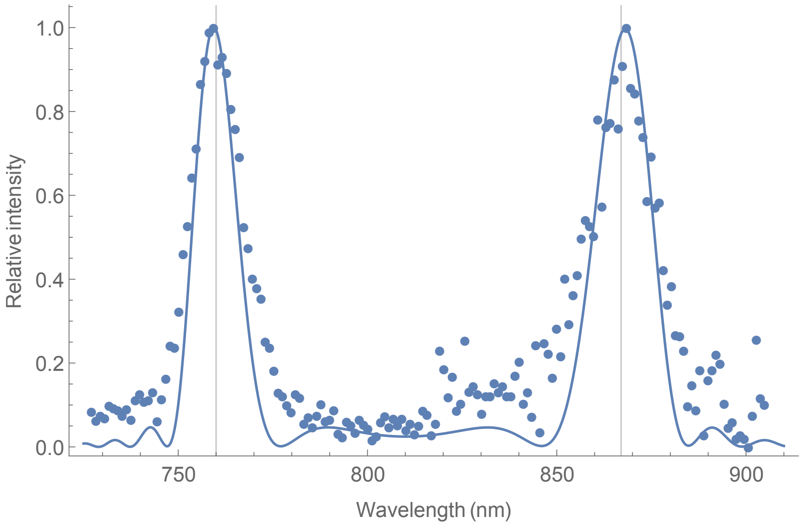

Figure 3.8: Relative intensity of spectrum from Tang (dots) and the modeled spectrum with maximum emission angle 0.2° (line)

The crystal tilt angle that satisfies the collinear phase matching conditions for the target wavelengths was first determined. The maximum accepted emission angle was then varied while attempting to match the peak wavelength of the signal to that of the measured data. From the data, the measured spectrum had peaks at roughly 759.5 nm and 869.0 nm and for the model, a maximum emission angle of 0.2° was used to shift the peaks to 759.4 nm and 868.1 nm. This is a reasonably good agreement with the measured spectrum for the signal (760 nm) peak while the comparatively poorer fit for the idler (867 nm) peak can be explained by the lower sensitivity of the spectrometer at that wavelength region.

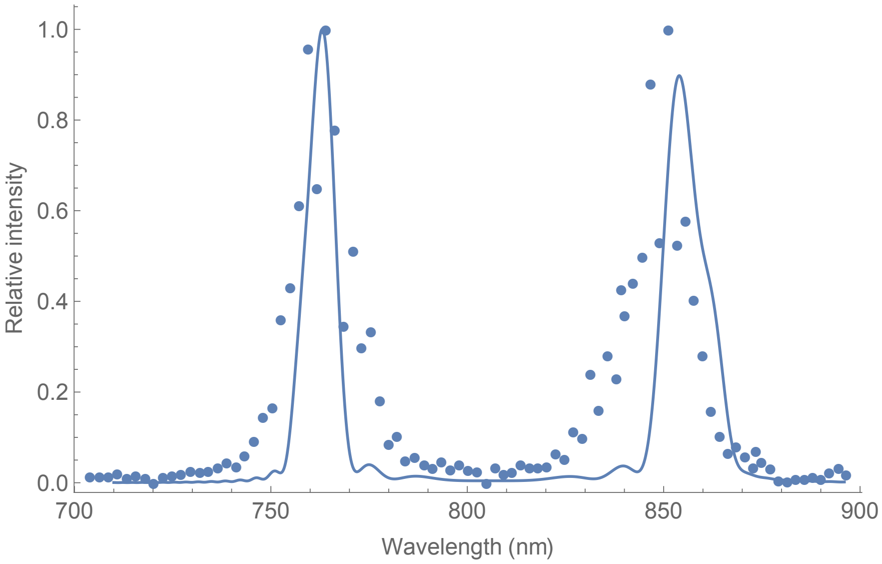

FIGURE 3.9: Relative intensity of spectrum from Trojek (dots) and the modelled spectrum with maximum angle 0.4° (line)

The second source that will be analysed is from Trojek [36], which has a crystal length of 15.76 mm, target wavelength of 765 nm and 850 nm and pump wavelength of 403 nm. A similar treatment is used as in the first source and the measured data, the best fit from the model is shown in Figure 3.9.

The fit was done with maximum emission angle of 0.4° which gave the peak wavelengths of 763.1 nm and 853.9 nm, as opposed to the reported central wavelengths of 762.8 ± 0.4 nm and 849.4 ± 0.6 nm. Although there is still a significant difference in the signal wavelength that was measured and modeled, it was found that increases of the maximum emission angle beyond 0.4° did not significantly shift the peak wavelength. The agreement between the model and measured value for the signal (765 nm) peak is again better than the idler (850 nm) peak.

It was noticed that the width of the peaks from the model for both sources were smaller than that suggested by the measured data. This could be due to the uncertainty from the spectral resolution of the spectrometers used and can be taken into account by doing a convolution of the modeled peaks $f(x')$ with an instrument response function $g(x')$. The convolution integral is then given as

$$h(x) = \int_{-\infty}^{\infty} f(x')g(x-x')\,dx'$$

For both sources we use a Gaussian response function with a standard deviation of 0.5 nm. The resulting peaks fit the experimental data better and are shown in Figure 3.10

for the first source and Figure 3.11 for the second. This allows the uncertainty of the spectrometer to be estimated.

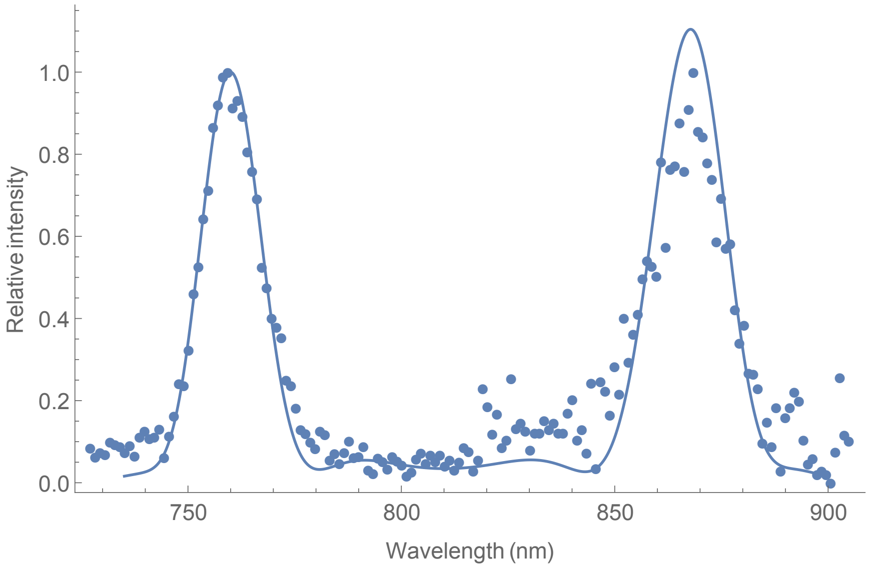

FIGURE 3.10: Relative intensity of spectrum from Tang (dots) and the convoluted spectrum with a Gaussian function of standard deviation 0.5 nm (line)

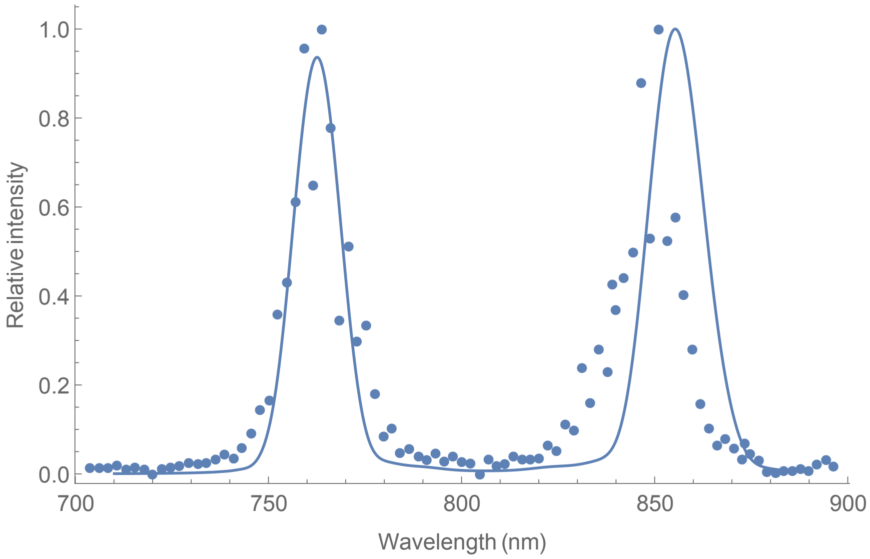

FIGURE 3.11: Relative intensity of spectrum from Trojek (dots) and the convoluted spectrum with a Gaussian function of standard deviation 0.5 nm (line)

3.5 Extended source

One limitation of the model developed here is the assumption of a point source at the center of the crystal. Using Equation (2.9), the walk-off angle is 3.632° which, for a crystal of length 15.76 mm, translates to a transverse walk-off distance from the optical axis of 1.0006 mm. This is a large distance considering that the waist of the pump beam can be on the order of about 0.1 mm or less and thus will need to be accounted and compensated for. The down-converted light do not experience the walk-off effect as they have ordinary polarisation.

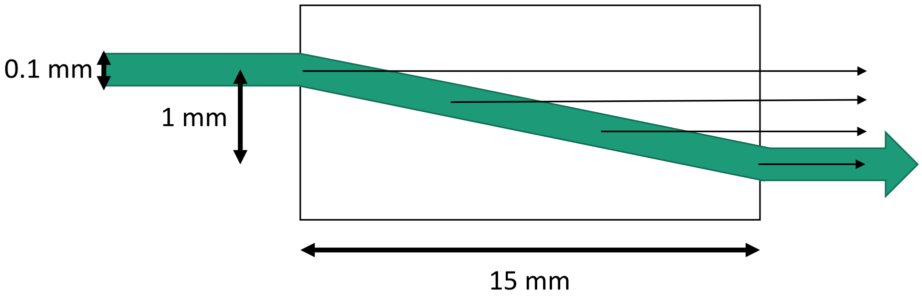

FIGURE 3.12: Down-converted beam (black arrows) gets generated throughout the pump beam's path (green arrow) in the crystal

The modified picture of the down-conversion in the crystal is shown in Figure 3.12. As the spatial walk-off effect occurs only in one direction, the down-converted beam is elongated in one transverse direction while the other remains unchanged. This suggests that adding a cylindrical lens, which focuses light in a single direction, could be the appropriate lens to use. Down-conversion occurs throughout the path of the pump beam in the crystal, but it is sufficient to consider only the rays on both ends of the elongated transverse direction of the down-converted beam at the exit face of the crystal (the ray along the optic axis and another ray 1 mm away from the optic axis). For the rays to be accepted into the fiber they have to end up within the acceptance cone of the fiber. We will check this using the ray transfer matrix method.

The ray transfer matrix method allows ray tracing within a plane to be done quickly. A ray is represented by a column vector consisting of its distance from the optical axis x and the angle it makes with the optical axis θ. Each part of the path of the ray, for example encountering a lens or just travelling through free space, is represented by a matrix that acts on the column vector to give the resultant parameters of the ray. The paraxial assumption is used and the matrices that will be used are:

$$\text{Free space: } \begin{pmatrix} 1 & d \\ 0 & 1 \end{pmatrix}, \text{ Spherical boundary: } \begin{pmatrix} 1 & 0 \\ -\frac{n_2-n_1}{n_2 R} & \frac{n_1}{n_2} \end{pmatrix}, \text{ Thin lens: } \begin{pmatrix} 1 & 0 \\ -1/f & 1 \end{pmatrix}$$

where d is the propagation distance, n_1, n_2 and R are the initial and final refractive index and radius of curvature of the spherical boundary, and f is the focal length of the cylindrical lens.

The achromatic doublet can be considered as three spherical surfaces separated by a short distance and the cylindrical lens treated as a thin lens. The ray tracing for the set up for our model is thus

$$\begin{pmatrix} x \\ \theta \end{pmatrix}_{\text{final}} = \begin{pmatrix} 1 & d_4 \\ 0 & 1 \end{pmatrix} \begin{pmatrix} 1 & 0 \\ \frac{1-n_3}{R_3} & n_3 \end{pmatrix} \begin{pmatrix} 1 & d_3 \\ 0 & 1 \end{pmatrix} \begin{pmatrix} 1 & 0 \\ \frac{n_3-n_2}{n_3 R_2} & \frac{n_2}{n_3} \end{pmatrix} \begin{pmatrix} 1 & d_2 \\ 0 & 1 \end{pmatrix}$$
$$\begin{pmatrix} 1 & 0 \\ -\frac{n_2-n_1}{n_2 R_1} & \frac{1}{n_2} \end{pmatrix} \begin{pmatrix} 1 & d_1 \\ 0 & 1 \end{pmatrix} \begin{pmatrix} 1 & 0 \\ -1/f & 1 \end{pmatrix} \begin{pmatrix} 1 & d_0 \\ 0 & 1 \end{pmatrix} \begin{pmatrix} x \\ \theta \end{pmatrix}_{\text{initial}}$$

with the various parameters defined in Figure 3.13.

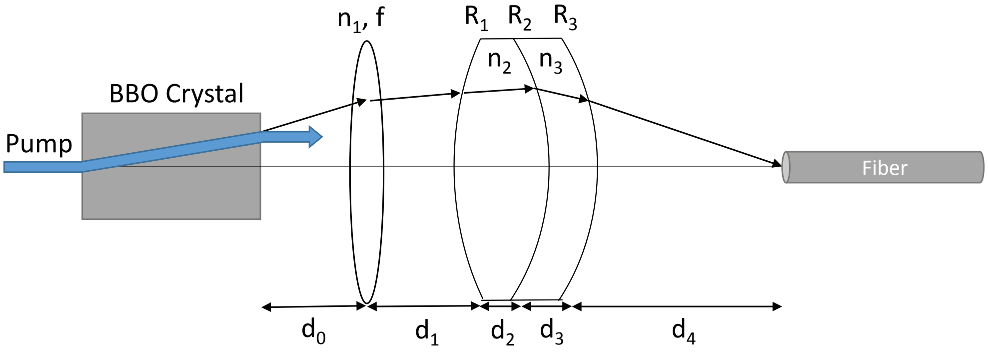

FIGURE 3.13: Diagram of extended source model showing the free parameters

We shall now find solutions using the AC080-020-B achromatic lens from Thorlabs that have the parameters

$$R_1 = 13.5mm,\ R_2 = 10.6mm,\ R_3 = 47.8mm$$
$$d_2 = 2.3mm,\ d_3 = 1.3mm$$
$$n_2 = 1.6431(\text{N-LAK22}),\ n_3 = 1.7853(\text{N-SF6HT})$$

and with a cylindrical lens with refractive index $n_1 = 1.5111$ (N-BK7). There is thus d_0, d_1, d_4 and f left to adjust.

We choose the parameters $d_0 = 5mm$, $d_1 = 400mm$, $f = 4mm$ and solve for

$$\mathbf{M} \begin{pmatrix} 1 \\ 0 \end{pmatrix} = \begin{pmatrix} 0 \\ k \end{pmatrix}$$

where **M** is the matrix of the system, k is unrestricted and the unit of distance is mm. d_4 is found to be 12.36 mm. To determine whether the rays lie within the acceptance cone of the fiber, we simply check that the distance from the optical axis x and the angle θ are less than the mode field diameter and the numerical aperture of the fiber respectively. Given the parameters above, the calculations show that all rays emitted at 0.2° or less will be accepted into a fiber of core diameter of 0.005 mm and numerical aperture of 0.15. We have thus shown that a cylindrical lens can provide some compensation for the walk-off of the pump beam. Further adjustments of the parameters and the focus length of the cylindrical lens can be done to improve the maximum emission angle that is accepted into the fiber.

Chapter 4

Conclusion

We have developed a model of a collinear type I non-degenerate SPDC correlated photon source together with the collection optics that couple the down-converted light into a fiber. A classical plane wave treatment was used in the derivation of the down-conversion with the further assumption of a point source for the down-converted emission within the crystal. These assumptions admittedly make the model a little unrealistic, however the model is still able to capture several features of the source, such as the shift of peak wavelengths with increasing collection beam divergence angle.

With this model, and given the pump and collection beam parameters, we can predict the relative intensity of the wavelengths that are detected. A comparison was done with the spectrum of two sources. Shifts of the peak wavelengths in the measured spectrum from the targetted values were observed and matched with the peak wavelengths produced by the model by changing the collection beam divergence angle. Thus the divergence angle of the collection beam used in the sources could be estimated. Similarly, the widths of the peaks were matched to that of the model by convoluting the modeled peaks with a Gaussian function and varying the standard deviation of the response function, thus allowing the estimation of the error of the spectrometer.

Spatial walk-off effects can be significant for tightly focused beams with small spot sizes. This will reduce the coupling efficiency of the down-converted beam into the fiber. To compensate for this, the addition of a cylindrical lens was studied and appropriate parameters were found to correct for emission angles of up to 0.2°. Further efforts to improve the model could focus on finding better methods of correction for the walk-off effects to allow for a wider range of emission angles to be accepted. Another possible area to work on is to allow for Gaussian pump beam modes. An approximate way of achieving this is to treat the Gaussian beam as being made of many plane waves, each within a small volume. The down-conversion spectrum can then be calculated at points within crystal and integrated together. With these modifications, the applicability of the model to the experimental set up would be much improved.

Appendix A

Numerical methods

This section will provide brief descriptions of the numerical methods used in finding the roots of equations and definite integral of a function that are used in this project.

A.1 Newton-Raphson method

The Newton-Raphson method is an iterative root-finding process for real-valued functions. This method starts off with a guess of the root x_0. The intersection between the tangent line of the function at $f(x_0)$ and the x-axis is found, and this new guess for the root x_1 is used for the next iteration. In this way, successive guesses x_n converge towards the root and the iteration is ended when the $f(x_n)$ is smaller than a chosen tolerance.

Assuming we start with a guess that is close to the root so that $(x_1 - x_0)$ is small, where x_1 is the next guess for the root of the function, and $f(x_1 - x_0)$ can be expanded in a Taylor series

$$f(x_1) \approx f(x_0) + (x_1 - x_0)f'(x_0)$$

Since we require $f(x_1) = 0$, we can solve for x_1:

$$x_1 = x_0 - \frac{f(x_0)}{f'(x_0)}$$

For the ith iteration,

$$x_{i+1} = x_i - \frac{f(x_i)}{f'(x_i)}$$

and the derivative of a function $f'(x)$ can be found using the finite difference approximation

$$f'(x) \approx \frac{f(x+h) - f(x)}{h}$$

where h is a small number.

This method does not necessarily converge to the root and so the starting guess should be carefully chosen to be close to the actual root.

A.2 Trapezoid rule

The trapezoid rule is a method of approximating the definite integral of a function where the area under the function is split into n equally spaced trapeziums of width h (Figure A.1). The integral can then be approximated by adding up the area of all the trapeziums

$$\begin{aligned}\int_a^b f(x)\,dx &\approx \sum_n \frac{f(x_n+h) + f(x_n)}{2}\,h \\ &= h\left(\frac{1}{2}f(x_1) + f(x_2) + \ldots + f(x_n) + \frac{1}{2}f(x_n+h)\right)\end{aligned}$$

where x_n is the x-coordinate of the nth trapezium and $h = (b-a)/n$.

The accuracy of the integral increases with the number of trapeziums n and can be estimated by recalculating the integral with double the number of trapeziums and then checking the two calculated values for differences in the digits within the desired number of significant figures.

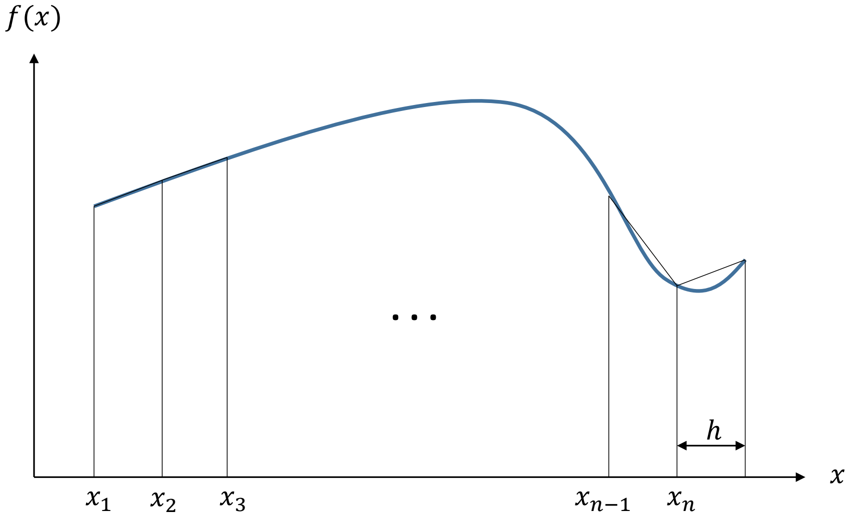

FIGURE A.1: Area under a function approximated by the sum of n equally spaced trapeziums

Bibliography

[1] Gregor Weihs, Thomas Jennewein, Christoph Simon, Harald Weinfurter, and Anton Zeilinger. Violation of bell's inequality under strict einstein locality conditions. *Physical Review Letters*, 81(23):5039, 1998.

[2] Dik Bouwmeester, Jian-Wei Pan, Klaus Mattle, Manfred Eibl, Harald Weinfurter, and Anton Zeilinger. Experimental quantum teleportation. *Nature*, 390(6660): 575–579, 1997.

[3] Thomas Jennewein, Christoph Simon, Gregor Weihs, Harald Weinfurter, and Anton Zeilinger. Quantum cryptography with entangled photons. *Physical Review Letters*, 84(20):4729, 2000.

[4] TB Pittman, YH Shih, DV Strekalov, and AV Sergienko. Optical imaging by means of two-photon quantum entanglement. *Physical Review A*, 52(5):R3429, 1995.

[5] Alois Mair, Alipasha Vaziri, Gregor Weihs, and Anton Zeilinger. Entanglement of the orbital angular momentum states of photons. *Nature*, 412(6844):313–316, 2001.

[6] Leonardo Neves, G Lima, JG Aguirre Gómez, CH Monken, C Saavedra, and S Pádua. Generation of entangled states of qudits using twin photons. *Physical review letters*, 94(10):100501, 2005.

[7] Julio T Barreiro, Nathan K Langford, Nicholas A Peters, and Paul G Kwiat. Generation of hyperentangled photon pairs. *Physical review letters*, 95(26):260501, 2005.

[8] Alexander Ling, Antia Lamas-Linares, and Christian Kurtsiefer. Absolute emission rates of spontaneous parametric down-conversion into single transverse gaussian modes. *Physical Review A*, 77(4):043834, 2008.

[9] Ryan S Bennink. Optimal collinear gaussian beams for spontaneous parametric down-conversion. *Physical Review A*, 81(5):053805, 2010.

[10] Morgan W Mitchell. Parametric down-conversion from a wave-equation approach: Geometry and absolute brightness. *Physical Review A*, 79(4):043835, 2009.

[11] Jean-Loup Smirr, Matthieu Deconinck, Robert Frey, Imad Agha, Eleni Diamanti, and Isabelle Zaquine. Optimal photon-pair single-mode coupling in narrow-band spontaneous parametric downconversion with arbitrary pump profile. *JOSA B*, 30 (2):288–301, 2013.

[12] Hannah E Guilbert and Daniel J Gauthier. Enhancing heralding efficiency and biphoton rate in type-i spontaneous parametric down-conversion. *IEEE JOURNAL OF SELECTED TOPICS IN QUANTUM ELECTRONICS*, 21(3):6400610, 2015.

[13] JA Armstrong, N Bloembergen, J Ducuing, and PS Pershan. Interactions between light waves in a nonlinear dielectric. *Physical Review*, 127(6):1918, 1962.

[14] Nicolaas Bloembergen and PS Pershan. Light waves at the boundary of nonlinear media. *Physical Review*, 128(2):606, 1962.

[15] Geoffrey New. *Introduction to Nonlinear Optics*. Cambridge University Press, 2011.

[16] David C Hutchings. Applied nonlinear optics.

[17] Peter E Powers. *Fundamentals of nonlinear optics*. CRC Press, 2011.

[18] Max Born and Emil Wolf. *Principles of optics: electromagnetic theory of propagation, interference and diffraction of light*. Cambridge university press, 1999.

[19] AV Smith, DJ Armstrong, and WJ Alford. Increased acceptance bandwidths in optical frequency conversion by use of multiple walk-off-compensating nonlinear crystals. *JOSA B*, 15(1):122–141, 1998.

[20] Jean-Jacques Zondy, Christophe Bonnin, and Dominique Lupinski. Second-harmonic generation with monolithic walk-off-compensating periodic structures. i. theory. *JOSA B*, 20(8):1675–1694, 2003.

[21] Richard L Sutherland. *Handbook of nonlinear optics*. CRC press, 2003.

[22] PA Franken, AE Hill, CW Peters, and G Weinreich. Generation of optical harmonics. *Physical Review Letters*, 7(4):118–119, 1961.

[23] Andreas Christ, Alessandro Fedrizzi, Hannes Hubel, Thomas Jennewein, and Christine Silberhorn. *Chapter 11 - Parametric Down-Conversion*, volume 45 of *Experimental Methods in the Physical Sciences*. Academic Press, 2013.

[24] Charles C Wang and George W Racette. Measurement of parametric gain accompanying optical difference frequency generation. *Applied Physics Letters*, 6(8): 169–171, 1965.

[25] SE Harris, MK Oshman, and RL Byer. Observation of tunable optical parametric fluorescence. *Physical Review Letters*, 18(18):732–734, 1967.

[26] David C Burnham and Donald L Weinberg. Observation of simultaneity in parametric production of optical photon pairs. *Physical Review Letters*, 25(2):84, 1970.

[27] WH Louisell, A Yariv, and AE Siegman. Quantum fluctuations and noise in parametric processes. i. *Physical Review*, 124(6):1646, 1961.

[28] TG Giallorenzi and CL Tang. Quantum theory of spontaneous parametric scattering of intense light. *Physical Review*, 166(2):225, 1968.

[29] DA Kleinman. Theory of optical parametric noise. *Physical Review*, 174(3):1027, 1968.

[30] GD Boyd and DA Kleinman. Parametric interaction of focused gaussian light beams. *Journal of Applied Physics*, 39(8):3597–3639, 1968.

[31] Paul G Kwiat. Hyper-entangled states. *Journal of modern optics*, 44(11-12):2173–2184, 1997.

[32] Julio T Barreiro, Nathan K Langford, Nicholas A Peters, and Paul G Kwiat. Generation of hyperentangled photon pairs. *Physical review letters*, 95(26):260501, 2005.

[33] Andreas Christ and Christine Silberhorn. Limits on the deterministic creation of pure single-photon states using parametric down-conversion. *Physical Review A*, 85 (2):023829, 2012.

[34] Pavel Trojek. Efficient generation of photonic entanglement and multiparty quantum communication. 2007.

[35] Paul G Kwiat, Edo Waks, Andrew G White, Ian Appelbaum, and Philippe H Eberhard. Ultrabright source of polarization-entangled photons. *Physical Review A*, 60(2):R773, 1999.

[36] Pavel Trojek and Harald Weinfurter. Collinear source of polarization-entangled photon pairs at nondegenerate wavelengths. *Applied Physics Letters*, 92(21):211103, 2008.